NSG 7092

(NASA-CR-169379) THE IMPULSIVE PHASE OF SOLAR FLARES. 2: CHARACTERISTICS OF THE HARD X-RAYS (Stanford Univ.) 48 p
HC A03/MF A01 CSCL 03B

N82-34328

Unclas
G3/92 35371

THE IMPULSIVE PHASE OF SOLAR FLARES
II. CHARACTERISTICS OF THE HARD X-RAYS

John Leach[1] and Vahé Petrosian[1]
Institute for Plasma Research
Stanford University
Stanford, CA

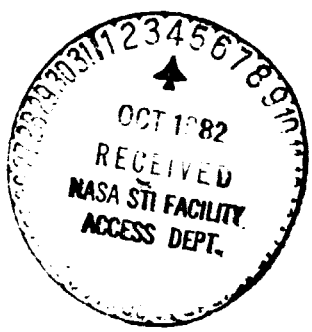

[1]Also Department of Applied Physics

Abstract

We use the results of our investigation into the electron distribution in the general non-thermal models of solar flares to calculate the characteristics of the impulsive hard x-rays. We look at the height distribution, the spectrum, the polarization and directivity of the x-rays and investigate how these x-ray characteristics are affected by the parameters defining the model. We obtain an expression for the x-ray intensity as a function of source height which is an excellent fit under certain constraints which are discussed. We then look at some recently available data with spatial resolution and show that we are able to reproduce these data adequately with our non-thermal model and to determine the values of the parameters describing the flares.

INTRODUCTION

One resource from which we are able to gain information as to the nature of the accelerated electrons in a flare is observations of hard x-rays. The theory describing the generation of bremsstrahlung radiation from electrons is well understood (for references see the review by Brown 1975; and Kane et al. 1980), but there are still many difficulties to be overcome when inverting the problem (Craig and Brown 1976). There are many free parameters involved when we attempt to infer electron characteristics from the observed x-rays. Many different electron distributions are able to mimic the same x-ray output if taken over a suitable flare volume.

Until recently most experiments were concerned with the spectrum of the x-rays. As a result, early work on flare modelling dealt with simplified assumptions about the characteristics of the electrons and the flare geometry (Hudson 1972; Brown 1972a, 1972b, 1973; Petrosian 1973, Kane 1974; Brown and McClymont 1975), with considerable attention devoted to the differences between the so-called thermal and non-thermal models. More recently these works have been elaborated upon by including the effects of a reverse current (Knight and Sturrock 1977; Hoyng and Melrose 1977; Emslie 1980;), the photospheric albedo (Santangelo, Horstman and Horstman-Moretti 1973; Langer and Petrosian 1977; Bai and Ramaty 1978) and a more thorough analysis of thermal models (Crannell et al. 1978; Brown, Melrose and Spicer 1979; Smith and Lilliequist 1979; Smith and Brown 1980; Brown and Hayward 1981; Emslie 1981).

In order to understand more precisely the role of the electrons in flares, we need to look at the x-rays in more detail. We need to look for information on the polarization and directivity of the x-rays and the height distribution of the x-rays throughout the flare loop.

The instruments available on SMM have made available not only data of high spectral resolution but also high spatial resolution (van Beek et al. 1980, 1981; Hoyng et al. 1981a, 1981b). Recent stereoscopic observations of limb flares have provided further data on spatial structure and directivity (Kane et al. 1979, Kane 1980; Kane et al. 1982). These, along with high spatial resolution microwave observations are giving us previously unavailable opportunities to understand flares.

Further insight into the flare problem might be gained from observations of x-ray polarizations. Earlier modelling showed that it should be easy to distinguish between flares with nearly isotropic electron distributions and having expected polarizations of a few percent and flares with beamed electrons having polarizations of up to 80 percent (Brown 1972b; Haug 1972; Henoux 1975; Langer and Petrosian 1977; Bai and Ramaty 1978). Unfortunately, there is no facility for making polarization measurements on board the SMM and past experiments have been inconclusive (Tindo, Shuryghin and Steffen 1976 and references cited within).

Our objective is to understand better the nature of the electron distribution in flares by calculating the x-rays to be expected according to a general non-thermal model and comparing

these results with the available data. To obtain a reliable x-ray distribution the transport of the electrons through the flare plasma must be treated accurately.

In a previous work (Leach and Petrosian 1981, hereafter referred to as Paper 1), we have described the evaluation of the electron transport for general non-thermal models. (We did not include reverse currents and, therefore, our results are best suited to low beam current densities or to high plasma density and temperature.) Here we use these results to obtain the characteristics of the x-rays. In Section II we discuss briefly the flare parameters and their relation to the expected bremsstrahlung radiation. In Section III we present some general results and in Section IV we compare these results with observations to set limits on some flare parameters. In Section V we summarize our conclusions.

II. GENERAL DESCRIPTION

X-rays of energy less than 1 MeV, generated during the impulsive phase of a solar flare, are the result of bremsstrahlung from electrons within that same energy range. In non-thermal models these electrons form a suprathermal beam moving through the background flare plasma. Most of the energy of the beam electrons goes into heating the ambient plasma with only a small fraction being radiated as x-rays. One consequence of this is that the evaluation of the x-ray characteristics can be performed separately from the analysis of the beam dynamics.

In paper 1 we described the model with which we followed the evolution of the electron beam through the plasma. We summarize it here (cf. Figure 1).

For simplicity we use a semi-circular flare loop above the transition region with a vertical extension below it. The magnetic field strength throughout the loop, B, is given as a function of a dimensionless column depth τ from the top of the loop. Electrons with a specified energy and pitch angle spectrum are injected at $\tau = 0$ and spiral along the magnetic field lines undergoing coulomb collisions with the ambient plasma and adiabatic scattering by the magnetic field variations. We use the Fokker-Planck formalism to evaluate the steady state electron distribution $f(E,\mu,\tau)$ with the injected spectrum $f_o(E,\mu)$ at $\tau = 0$. Here E and $\mu = \cos\alpha$ are the kinetic energy and pitch angle cosine of the electrons. With a knowledge of the electron distribution along the loop we can now proceed with the computation of the x-rays.

To compute the x-rays produced by the beam at any instant, consider an electron of energy E (momentum $\underline{P}$) at an instantaneous depth τ. The electron is scattered and emits an x-ray of energy k at an angle η to the direction $\underline{P}$. The photon is linearly polarized (Gluckstern, Hull, and Breit 1953) with its polarization vector either in the plane of emission (the $\underline{p},\underline{k}$ plane) or perpendicular to it. The cross sections for the production of photons are $d\sigma_{||}(p,k,\eta)$ and $d\sigma_{\perp}(p,k,\eta)$, respectively, and are given by Gluckstern and Hull (1953). To these cross sections we append the Elwert (1939) coulomb correction.

We are interested in the photon characteristics not in the plane of emission but in the overall frame of the whole flare. We define the global frame for the observations of x-rays to be the frame with the flare loop in the $\underline{y},\underline{z}$ plane and the photosphere (assumed to be flat) in the $\underline{x},\underline{y}$ plane (cf. Figure 2).

We are concerned with photons of energy k emitted in a direction with polar angle Θ and azimuthal angle Φ. We also characterize these photons using the four Stokes' parameters I, Q, U and V (Chandrasekhar 1960).

We need to be able to transform the Stokes' parameters from the instantaneous plane of emission (the $\underline{p},\underline{k}$ plane for the emitting electron) into the plane of observation (the $\underline{k},\underline{z}$ plane). As the bremsstrahlung radiation is linearly polarized, we need only concern ourselves with the first three Stokes' parameters, the fourth, V, being identically zero.

As an electron spirals along the magnetic field lines, the plane of emission is continually changing. At any instant the angle ψ between the plane of emission and the plane of observation is given by

$$\cos\psi = \left(\frac{\underline{p}\wedge\underline{k}}{|\underline{p}\wedge\underline{k}|}\right)\cdot\left(\frac{\underline{k}\wedge\underline{z}}{|\underline{k}\wedge\underline{z}|}\right) \quad . \qquad (1)$$

Following Chandrasekhar we define the Stokes' parameters for the instantaneous beam of x-rays emitted relative to the plane of emission. For this beam the first two of these parameters are

$$i(p,k,\eta) \propto d\sigma_{\perp}(p,k,\eta) + d\sigma_{||}(p,k,\eta)$$

$$q(p,k,\eta) \propto d\sigma_{\perp}(p,k,\eta) - d\sigma_{||}(p,k,\eta) \qquad (2)$$

If we denote by $d\sigma_1(p,k,\eta)$ and $d\sigma_2(p,k,\eta)$ the cross sections for photons emitted with polarization vectors rotated 45^{o} from the perpendicular and parallel directions, then the third Stokes' parameter is

$$u(p,k,\eta) \propto d\sigma_1(p,k,\eta) - d\sigma_2(p,k,\eta) \quad . \qquad (3)$$

As shown by Haug (1972) the values of the three Stokes' parameters in the plane of observation (the primed quantities) are obtained by the transformation relaticns

$$\begin{aligned} i'(p,k,\eta) &= i(p,k,\eta) \\ q'(p,k,\eta) &= q(p,k,\eta) \cos 2\psi. \\ u'(p,k,\eta) &= u(p,k,\eta) \sin 2\psi. \end{aligned} \qquad (4)$$

The Stokes' parameters for the radiation of energy k in the direction (θ, Φ) from a depth τ is obtained by integrating over all the contributing electrons. We thus obtain

$$\begin{bmatrix} I \\ Q \\ U \end{bmatrix}_{\tau}(k,\theta,\Phi) = \int_{\mu=-1}^{1} d\mu \int_{\phi=0}^{2\pi} d\phi \int_{E=k}^{\infty} dE A(\tau)\, f(E,\mu,\tau)\, v(E)\, n(\tau) \begin{bmatrix} i' \\ q' \\ u' \end{bmatrix}(p,k,\eta) \qquad (5)$$

Integration of these equations over all depths τ will give the Stokes' parameters for the radiation from the whole loop. Here ϕ is the azimuthal angle of the electron about the magnetic field line, $A(\tau)$ is the cross sectional area of the loop at the depth τ, $v(E)$ is the velocity of the electron of energy E and $n(\tau)$ is the number density of ambient plasma protons at depth τ. The relationships between the direction (θ, ϕ) and the angles χ and ψ are complex functions of the electron's pitch angle $\alpha = \cos^{-1}\mu$, azimuthal angle ϕ and the direction of the magnetic field relative to the z axis.

To analyze the height distribution of the x-rays from our models, we divide the flare loop into adjoining segments, each a small arc of the coronal loop or a part of the vertical chromospheric loop. In this case we find it more informative to use Stokes' parameters given with respect to frames other than the global frame which is the one that we use when we consider the radiation from the whole flare.

For each segment the integration of eq. 5 over the appropriate range of values of τ can be simplified as follows. For each segment we define a mean magnetic field direction $\underline{B}_i$ (say, in the direction of the field at the center of the segment; cf. Figure 1). We take this to be the polar direction for the i^{th} segment and evaluate the Stokes' parameters of the individual

segment in the (local) $\underline{k},\underline{B}_i$ plane. For a sufficiently short segment in which the curvature of the magnetic field would be negligible, we would have azimuthal symmetry of the electron distribution about the field direction $\underline{B}_i$. In this case the third Stokes' parameter would be identically zero (Haug 1972). For our curved segments (cf. Figure 1) the electron distribution will be close to being azimuthally symmetric about the polar direction and, consequently, the value of the Stokes' parameter U will be negligible.

For each segment, then, we can use the Stokes' parameters to obtain the directivity and the degree of linear polarization. Let

$$\bar{I}_i(k) = (1/4\pi)\int_{\theta=0}^{\pi}\int_{\phi=0}^{2\pi} I_i(k,\theta,\phi)\sin\theta\, d\theta\, d\phi \qquad (6)$$

be the average value of $I_i(k,\theta,\phi)$ in the i^{th} loop segment. We then define the directivity $D_i(k,\theta,\phi) = I_i(k,\theta,\phi)/\bar{I}_i(k)$ and the degree of polarization

$$\pi_i(k,\theta,\phi) = \frac{[Q_i(k,\theta,\phi)^2 + U_i(k,\theta,\phi)^2]^{1/2}}{I_i(k,\theta,\phi)} \qquad (7)$$

The inclination of the major axis of the ellipse of polarization vectors to the plane of observation, the $\underline{k},\underline{B}_i$ plane is given by

$$\omega_i(k,\theta,\phi) = (1/2)\tan^{-1}\left\{\frac{U_i(k,\theta,\phi)}{Q_i(k,\theta,\phi)}\right\} \qquad (8)$$

and as U_i is small relative to Q_i, ω_i is close to zero or to $\pi/2$ according to whether Q_i is positive or negative. Thus, the direction of linear polarization is close to being either in the plane or perpendicular to it.

III. RESULTS

In this section we present some general results on the spectrum, directivity and polarization of the x-rays and on the variation of these with height through the loop for the general non-thermal models. As shown in paper 1, these models are classified by the spectrum and pitch angle distribution of the electrons and the parameter $d\ln B/d\tau$ along the loop. We inject electrons with a power law spectral index δ and a gaussian distribution in pitch angles;

$$F_o(E,\mu) = A\, E^{-\delta} \exp\left\{ -\alpha^2/\alpha_o^2 \right\} \qquad (9)$$

The Fokker-Planck method gives the electron distribution throughout the loop: $F(E, \mu, \tau)$, and equation (5) gives the variation with τ of the Stokes' parameters and therefore gives a complete description of the characteristics of the x-rays.

The x-ray results may then be classified according to the three parameters $d\ln B/d\tau$, δ and α_o^2. We shall be describing the results for a selection of nine models which allow us to observe the dependence of the x-rays on each of the three parameters. The models are given in Table 1.

As is evident from equation (5), at each level τ the x-ray spectrum is that of a thin-target model for the appropriate electron distribution at that level. In particular, around $\tau = 0$ (i.e., at the top of the loop) where the electron distribution is very close to the injected spectrum (equation 9), we expect an x-ray spectrum with spectral index $\gamma \simeq \delta + 1.0$ (cf., e.g., Brown 1971). On the other hand, the spectrum of the spatially unresolved (i.e., integrated over all τ) x-rays should be the spectrum of a thick target model (cf., e.g., Brown 1972b and paper 1, eqs. 23 to 25) with $\gamma \simeq \delta - 1/2$. The last two columns of Table 1 give $\gamma_{top} - \delta$ and $\delta - \gamma_{total}$ for the nine models. As can be seen, the values of $\gamma_{top} - \delta$ are very near to their expected value of 1.0. Any deviation can be accounted for by the uncertainty in the determinations of γ_{top} (taking a best power law fit introduces an uncertainty of approximately 0.1) and by the finite column depth of the top segment. The values of $\delta - \gamma_{total}$ deviate from their expected value of 0.5 consistently with the rate of convergence of the magnetic field. This arises from uncertainties in the determinations of γ_{total} and because the expected values are approximations valid primarily for uniform magnetic fields.

This is one test of the accuracy of the numerical program. We have also tested the numerical results further by comparing our results for a uniform and straight tube model with earlier semi-analytic results (Brown 1972b, Haug 1972 and Langer and Petrosian 1977). These works did not take into account the dispersion in pitch angles of the electrons. Therefore, they give results which can serve as order-of-magnitude indicators of

the polarization and directivity. With these we find good agreement.

A. Integrated X-Rays

Before we present the results for the variation of the spectrum, directivity and polarization with τ, we shall describe briefly these characteristics for the x-rays integrated over the whole loop. We do this as most of the observations collected so far have not resolved the bursts spatially.

1) Spectrum. As mentioned above, the total spectrum is essentially that of a thick target, as shown in Table 1.

2) Directivity. Figure 3 shows the expected spectra as viewed from three directions: x, y and z for models 3 and 5. The effect on any of the spectra from the possible variation of the parameters α_o^2 and $d\ln B/d\tau$ would be small and no more than the uncertainty from the fitting of a best-fit power law.

Figure 4 shows the variation with θ of the x-ray directivity at 22 keV and 210 keV for models 3, 5 and 9. In all cases the x-rays are emitted primarily into the downward-facing hemisphere. The degree of beaming is less for models with larger α_o^2 or $d\ln B/d\tau$ as the electron distribution is more nearly isotropic for these models.

3) Polarization. In Figure 5 we show the variation of the photon polarization (in the y direction) with θ at photon energies of 16, 50 and 102 keV. As expected, model 3 with large α_o^2 and model 8 with large $d\ln B/d\tau$ have smaller degrees of polarization than model 5. In comparison though with Figures 2 and 3

of Langer and Petrosian (1977), our polarizations are small. This is because we have a loop rather than a straight tube and because we have included the effects of both pitch-angle diffusion and, for model 8, magnetic trapping in our analysis.

B. Variation with Depth

We now present the variation with τ of the x-ray parameters for the models in Table 1.

The variation with height or depth along the loop can be obtained once the variation of the ambient density along the loop is specified: $d\tau = 2 \times 10^{-23} n(s)ds$ (cf. paper 1). We will be using such a relationship in the next section when we compare our results with observations.

1) Spectrum. At each height the spectrum of the x-rays integrated over both angles θ and Φ is, in general, a representative spectrum. This is especially true at low energies where the relativistic beaming effects are insignificant. In Figure 6 we show spectra at various values of τ throughout the loop for models 1, 3, 5 and 9. Also shown is the spectrum for the whole loop.

The variation of the spectrum from a thin target spectrum at the top towards a thick target spectrum for the whole loop is clearly evident in these figures.

2) Relative Intensity. The rate at which the beam generates photons depends upon the electron distribution and thus on the three input parameters δ, α_o^2 and $d\ln B/d\tau$. We define the

x-ray intensity as $I(k, \tau)$, the fraction of the total counts emitted per unit column depth at a depth τ and at photon energy k. Figures 7 through 9 show the variation of $I(k,\tau)$ with τ and the effects of the input parameters.

Figure 7 give $I(k, \tau)$ versus τ at k = 16 and 50 keV and for models 1, 2 and 3. The intensity is approximately constant for $\tau / k^2 << 1$. For $\tau / k^2 >> 1$, the intensity decreases rapidly (approximately as a power law in τ), because, as shown in paper 1, tne flux of electrons responsible for photons of energy k (that is, electrons with energy $E \gtrsim k$) decreases rapidly when $\tau/E^2 >> 1$. For large τ/k^2 we obtain $d\ln I/d\ln\tau = -\delta/2$, independent of k. That we expect this type of dependence of lnI on $\ln\tau$ can be seen with reference to the results of paper 1. Note that

$$I(k, \tau)\, d\tau = \int_{E=k}^{\infty} F(\tau, E)\ d\sigma(E,k)\ dE d\tau \quad . \qquad (10)$$

From equation 21 of paper 1 we see that the τ dependence of $F(\tau,E)$ is of the form $(1 + \tau\,(E+1)/E^2)^{-\delta/2 - 1/2}$. If we approximate the cross section by a delta function, i.e., $d\sigma(E,k) = \delta(k-E)$, then $I(k,\tau) \propto (1 + \tau\,(k+1)/k^2)^{-\delta/2 - 1/2}$. If, alternately, the cross section is taken as being approximately constant, we obtain

$$I(k, \tau)\, d\tau \propto \int_{E=k}^{\infty} F(\tau, E)\, dE\, d\tau \quad .$$

It can then be seen that for large values of $\tau(k+1)/k^2$, these extreme assumptions about the cross section give $d\ln I/d\ln\tau = -\delta/2 - 1/2$ and $-\delta/2 + 1/2$ respectively. We obtain a constant value for $d\ln I/d\ln\tau$ at large $\tau(k+1)/k^2$ which lies within these limits.

For all photon energies in our range from 10 keV to 210 keV, we find that the results of models 1, 2 and 3 are very well approximated at large depths by the form $I(k,\tau) \propto (1+\tau(k+1)/k^2)^{-\delta/2}$. Writing $I(k,\tau) = a(\delta,k)\,(1+\tau(k+1)/k^2)^{-\delta/2}$ and recalling that $I(k,\tau)$ is, by its definition, normalized, integrating over τ from $\tau = 0$ to $\tau = \infty$ gives the relationship

$$a(\delta,k) = (\delta/2 - 1)\left[(k+1)/k^2\right] \quad .$$

We, therefore, obtain the form

$$I(k,\tau) = (\delta/2 - 1)\left[(k+1)/k^2\right](1+\tau\,(k+1)/k^2)^{-\delta/2} \quad . \quad (11)$$

Though equation 11 was obtained based on the behavior of $I(k,\tau)$ at large τ, we find that it can be very accurate for small τ and all photon energies with some appropriate constraints on the parameters α_o^2 and $d\ln B/d\tau$.

In Figure 8 we show the effect of the parameter α_o^2. The amount of energy that an electron radiates as it travels unit distance measured parallel to the magnetic field depends inversely on the electron's pitch angle. Thus, as a narrow beam rapidly broadens within the plasma, the photon counts per unit τ can, initially, increase. Figure 8 clearly shows this effect. Also mentioned in paper 1 was the tendency of the electron beam, below depths where $\tau/E^2 \simeq 1$, to have lost any

information as to its pitch-angle distribution at $\tau = 0$. Thus below a depth where $\tau/k^2 \simeq 1$, the x-ray intensity profiles for different α_o^2 are essentially identical. A consequence of all this is that equation 11 can be accurately extended towards $\tau = 0$ for beams with $\alpha_o^2 \gtrsim 0.3$ and is accurate for all beams below a depth $\tau/k^2 \simeq 1$ (corresponding to a column depth of 2×10^{19} cm^{-2} for 10 keV photons).

In Figure 9 we show the effect of magnetic trapping on the x-rays. We specify a constant $d\ln B/d\tau$ throughout the coronal loop but do not continue it below the transition zone. Thus the magnetic trapping is all coronal trapping. Figure 9 shows that a relatively small increase in the strength of the magnetic field within the loop can cause a large increase in the x-ray intensity in the coronal loop. It only requires a moderate degree of trapping (a fivefold increase in the magnetic field strength within the coronal part of the loop is sufficient) to increase the intensity at the top of the loop by an order of magnitude. Thus the distribution of low-energy hard x-rays throughout the loop (energies of 10 to 20 keV, say, such as are imaged by HXIS) is particularly sensitive to even small amounts of coronal trapping.

3) Directivity and Polarization. To obtain large x-ray directivities and polarizations, it is necessary to have a highly collimated electron beam. Conversely, a nearly isotropic electron distribution will give rise to x-rays of negligible directivity and polarization.

In Figures (10) and (11) we show the directivity and polarization at 16 and 102 keV at several heights for model (5), which

has the most strongly collimated electron beam and a uniform magnetic field and, consequently, gives the largest directivities and degrees of polarization.

To facilitate the discussion of the results, we define a directivity ratio D, which is the ratio of the maximum to minimum directivities at a given height for a given photon energy. The directions of maximum and minimum directivity are usually antiparallel.

As can be seen for model (5), at the top of the coronal loop the x-rays are highly polarized and most highly directed. The directivity ratios at 16 keV and 102 keV are approximately 9 and 40, respectively, with the x-rays beamed primarily in the same direction as the electrons. The degree of linear polarization reaches a maximum of 85 percent for both energies in a direction normal to the direction of the electron beam.

We find that, throughout all our models, the values for the polarization and directivity are essentially independent of the azimuthal angle in the observation frame. This is one of the rewards of using the local observation frames, as described in Section II.

At the bottom of the coronal loop, at a column depth of 3 x 10^{18} cm^{-2} (τ/k^2 = 0.06 for k = 16 keV, = 0.002 for k = 102 keV), the x-rays are still highly directed. The directivity ratios are 7 and 40 at 16 keV and 102 keV, respectively. The degree of linear polarization is still high at 70 percent to 82 percent for the two energies shown. It is not until a column depth of approximately 10^{20} cm^{-2} ($\tau/k^2 \simeq 2.0$ for 16 keV) is reached that the x-rays start to become significantly more isotropic; both the

directivity and polarization fall as the source moves deeper into the chromosphere. At a depth of $\tau/k^2 \simeq 2.0$, the directivity ratios have fallen to 2 and 9 for 16 and 102 keV photons, respectively; and the degrees of polarization are 9 percent and 20 percent, respectively.

In contrast to model (5), which gives the largest directivity and polarization, model (3) has an injected beam which is isotropic in the forward pitch angles; and model (8) has a strongly converging coronal magnetic field.

For model (3) (Figure 12) the directivity ratio for 16 keV photons coming from any depth within the loop does not exceed a value of 2, and for 102 keV photons does not exceed a value of 6. The x-rays from the top of the coronal loop are about 30 percent polarized at all energies from 16 keV through to 102 keV. The polarization falls only slowly throughout the coronal loop, but then falls rapidly in the denser chromosphere. The polarization has fallen to 6 percent for 16 keV photons by the time the source has reached a column depth of 10^{20} cm^{-2}, and to 10 percent for 102 keV photons for a source at or below a depth of 10^{21} cm^{-2}. Looking at the loop as a whole the polarization is about 10 to 15 percent for a broad range of photon energies.

In model (8) (Figure 13) the strongly converging coronal magnetic field rapidly broadens and reflects the electron beam. In the corona the photons are nearly isotropic, being only slightly directed either parallel or antiparallel to the initial electron beam. The degree of polarization increases slightly with depth within the corona. This then falls as the source

moves into the chromosphere. The average degrees of polarization for the whole loop are 7 percent at 16 keV and 15 percent at 102 keV.

IV. OBSERVATIONS

In this section we compare the results described in the previous section with observations which have spatially resolved the x-ray bursts. Our aim is to use the observations to put limits on the model parameters and thus to come up with models which fit the observations. Firstly we need to convert our results from variations with column depth τ into variations with height. We do this by specifying the variation of the density throughout the loop. We assume a constant density from the top of the loop to the top of the transition region, which is at a column depth of N_{TZ}. Below the loop we have a thin transition region with rapidly increasing density and below that a chromosphere with a density scale height Hn = 2000 km. We specify a constant dlnB/ds throughout the whole loop, where s is the distance measured in cm from the top. Since the coronal dersity is so much less than the chromospheric density and the length of the curved coronal loop is so much larger than the length of the vertical chromospheric section, the immedite effects of any magnetic field convergence are unimportant except for in the corona. The values of dlnB/dτ quoted refer to the coronal portion of the loop.

We now look at some recent observations by the HXIS experiment on board the S.M.M. (Hoyng et al. 1981a) and the steroscopic observations of Kane et al. (1979 and 1982).

A) The HXIS experiment has the best available spatial resolution but is limited to imaging x-rays of 30 keV or less. Because of the significant contamination from thermal soft x-rays at and below 10 keV, the interpretation of the HXIS results becomes more complicated. Furthermore, the effect of the photospheric albedo may be significant for these observations. In a subsequent paper (in collaboration with Steve Langer), we shall consider the albedo effect and comment on the HXIS results in more detail. Here we just point out that the fact that many of the x-rays even at low energies come from what are expected to be the footpoints of the loop indicates that low-energy electrons must be able to penetrate to those depths. In terms of our model, we can use the figures given in Table 1 of Hoyng et al. (1981a) to put an upper limit on the transition-zone column depth. The ratios of counts in region B to regions A and C require $N_{TZ} \lesssim 2 \times 10^{19}$ cm^{-2} for their flare of 10 April 1980.

B) Information on the spatial distribution of the x-rays can also be obtained by stereoscopic observations of partially occulted limb flares such as those obtained by Kane and his collaborators using the International Sun Earth Explorer 3 (ISEE 3) and the Pioneer Venus Orbiter (PVO). These observations do not have the resolution of the HXIS experiment but contain more spectral information and, being of limb flares, are not affected by the albedo effects. We now discuss two such flares.

1) Flare of 5 October 1978 (Kane et al. 1979). This flare was estimated to be 15° behind the limb for ISEE 3, which could therefore see those parts of the flare at altitudes of $h \geq 25{,}000$ km above the photosphere. The PVO was able to see this flare down to an altitude of $h \simeq 700$ km. This flare was also analyzed by Brown, Hayward and Spicer (1981) [hereafter referred to as BHS]. We use a similar model to analyze this flare, but with the use of our full-beam dynamics and fully relativistic photon cross sections, we are able to improve upon the model used by BHS.

In conjunction with the above height information, ISEE 3 observed a power-law photon spectrum with an index $\gamma_{ISEE} \simeq 5.0$ over the 5 to 50 keV range; while in the 50-500 keV range, the PVO observed $\gamma_{PVO} \simeq 3$. The total PVO flux above 50 keV is approximately 600 times the corresponding ISEE flux obtained by extrapolating the ISEE 3 spectrum to 500 keV. Alternately, extrapolating the PVO spectrum down to 5 keV would give a PVO to ISEE 3 flux ratio of 6 over the 5 to 50 keV range.

As shown in Table 1, the difference between the spectral index from the top of a loop and that for the whole loop is expected to be about 1.5. We find that if we use a narrow injected beam ($\alpha_o^2 = 0.03$) with $\delta = 3.9$ and have no magnetic trapping, we are able to obtain a best fit of $\gamma_{top} = 4.9 \simeq \gamma_{ISEE\ 3}$ and $\gamma_{tot} = 3.2 \simeq \gamma_{PVO}$. Considering the observational uncertainties, this is a satisfactory fit. Using the PVO/ISEE 3 flux ratio of 600, we now find that the column depth from the top of the loop down to the altitude $h = 25{,}000$ km must be close to 8×10^{18} cm^{-2}.

The column depth derived here is roughly a factor of three larger than that obtained by BHS. If we assume, with BHS, a length of 20,000 to 30,000 km for the segment of the loop above 25,000 km, we obtain a coronal density of 3×10^9 cm^{-3}. This higher density may alleviate some of the difficulties discussed by BHS regarding the flux-limiting role of the reverse current.

Having obtained our model, let us now look at the expected polarization. From the top (thin target) 8×10^{18} cm^{-2} of the loop, we expect very high degrees of polarization, i.e., 70 percent at 10 keV, increasing to 83 percent at 50 keV and falling to 60 percent at 210 keV. Had the ISEE 3 spacecraft been equipped with a polarization-measuring device, it could easily have detected such high polarizations. For the bulk of the loop as seen by PVO, the degrees of polarization at the same energies would have been 6, 10 and 10 percent, respectively. Obviously, then, stereoscopic polarization measurements could provide decisive further constraints on the models.

Had this flare been seen by the HXIS experiment, it would have appeared brighter by a factor of approximately 20 at the footpoints than at the top of the loop in the energy range 11.5 to 30 keV. This result is not incompatible with, for example, the observations of Hoyng et al. (1981a).

2) Flares of 5 November 1979 (Kane et al. 1982). In this series of observations, PVO saw three flares, one precisely on the limb, one 4.3 degrees behind the limb, and the third 4.8 degrees behind the limb. All three flares were in full view of ISEE 3. Though not all of the same size when seen by ISEE 3, the

three flares did appear to be congruent, that is, the spectral shape of each flare was essentially the same whether seen by ISEE 3 or PVO, and the sepctral shapes one flare to the next were similar. Because of this congruency, we may treat the three observations as if they were separate observations of one "typical" flare. We then have, with reference to Figure 3 of Kane et al. (1982), a rough estimate of the height distribution of 100 to 200 keV x-rays within our "typical" flare. The mean spectral index over this energy range is 3.15.

The third flare was sufficiently occulted that PVO could see only those parts of the flare which were at altitudes greater than 2500 km above the photosphere. The rapidly changing x-ray source brightness with height requires that the transition zone be located very close to this height.

The constraints which we need to satisfy then in constructing our model are:

(1) Ten percent of the x-ray counts in the 100 to 200 keV range come from altitudes above 2500 km, and 45 percent come from above 2000 km.

(2) The spectral index is the same above and below 2500 km and is taken to be approximately 3.15.

Taken together, these constraints are best satisfied by a model with a broad injected beam (α_o^2 greater than or of order of, say, unity), no coronal trapping and a column depth down to 2500 km of approximately 1.2×10^{20} cm^{-2}. The electron spectral index, δ, is $\simeq 3.45$.

Because the region above 2500 km has a substantial column depth, the polarizations it gives rise to are not much larger than those seen for the whole flare. The maximum degree of polarization is of the order of 20 percent for energies up to 100 keV. The degree of polarization for the flare as a whole is less than 10 percent for all energies greater than 10 keV.

Again, had HXIS imaged this "typical" flare, it would have seen a loop which was approximately 2.8 times as bright as the footpoints in the energy range 11.5 to 30 keV.

V. CONCLUSIONS

The two examples of the previous section serve to illustrate several points when one constructs models based on x-ray observations.

1) Observations of limb flares have the distinct advantage that they are not complicated by the contribution of the photospheric albedo.

2) Without any information on the height distribution of the x-rays, we can say little about the flare model parameters. As an absolute minimum we need spectral and flux information from two regions of the flare, as as is provided by occultation experiments. If the two regions have the same spectral index, as is the case in the second of our Kane observations, we cannot be as precise as is possible when we have thick and thin target indices. More information on the height distribution of x-rays is crucial for the further development of the models.

3) Polarization measurements in conjunction with height distribution data are important. We expect to see polarizations at a high enough level from the upper regions of a flare loop that it would be detectable using present-day technology. The detection of large x-ray polarizations would be strong support for the non-thermal model.

4) A moderate degree of convergence of the coronal magnetic field has a large effect on the height distribution of the x-rays. Any considerable rate of convergence for the coronal magnetic field coupled with a typical flare transition zone column depth would lead to large coronal fluxes of photons of all energies. At low energies the flux from the coronal loop would swamp that from the footpoints. At high energies the coronal flux would be considerably in excess of what we may be led to expect going by presently available results. Thus we may tentatively conclude that the strength of the magnetic field defining the coronal loop must be approximately constant. This is similar to the indicated results from analyses of high spatial resolution and microwave observations of flares (Petrosian 1982).

ACKNOWLEDGMENT

This work was supported by the National Aeronautics and Space Administration under Grant NSG 7092 and the National Science Foundation under Grant ATM 81-16989.

Table 1. Models

#	δ	$\frac{d\ln B}{d\tau}$	α_o^2	$\gamma_{top} - \delta$	$\delta - \gamma_{tot}$
1	3	0	∞	1.0	0.6
2	4	0	∞	1.0	0.5
3	5	0	∞	1.0	0.5
4	5	0	0.4	1.1	0.6
5	5	0	0.04	0.9	0.6
6	5	2.5×10^4	0.4	0.8	0.4
7	5	5×10^4	0.4	0.7	0.15
8	5	5×10^4	0.04	0.6	0.4
9	5	5×10^4	∞	0.9	0.0

Table 1. The models referred to in the text with the values of the three input parameters δ, $d\ln B/d\tau$ and α_o^2 which determine them. Also shown are the values of $\gamma_{top} - \delta$ and $\delta - \gamma_{tot}$, where γ_{top} is the photon spectral index in segment 1 and γ_{tot} is the spectral index for the whole flare. The value of $d\ln B/d\tau$ quoted is valid only for the coronal magnetic field. Values of 0, 2.5×10^4 and 5×10^4 correspond to 1, 5 and 25-fold increases in the magnetic field strength from the top of the loop to the transition zone, respectively. $\alpha_o^2 = \infty$ corresponds to a uniform distribution in pitch angle between $\mu = 0$ and $\mu = +1.0$.

REFERENCES

Bai, T., and Ramaty, R. 1978, Ap. J., 219, 705.

Brown, J. C. 1971, Solar Phys., 18, 489.

1972a, Solar Phys., 25, 158.

1972b, Solar Phys., 26, 441.

1973, Solar Phys., 31, 143.

1975, in I.A.U. Symposium 68, Solar, Gamma-, X- and EUV Radiation, ed. S. R. Kane (Dordrecht: Reidel).

Brown, J. C., and Hayward, J. 1981, Solar Phys., 73, 121.

Brown, J. C., Hayward, J. and Spicer, D. S. (BHS) 1981, Ap. J. (Letters) 245, L91.

Brown, J. C., and McClymont, A. N. 1975, Solar Phys., 41, 135.

Brown, J. C., Melrose, D. B., and Spicer, D. S. 1979, Ap. J., 228, 592.

Chandrasekhar, S. 1960, Radiative Transfer (New York: Dover), p. 24.

Craig, I. J. D., and Brown, J. C. 1976, Astro. Ap., 49, 239.

Crannell, C. J. et al. 1978, Ap. J., 223, 620.

Elwert, G. 1939, Ann. Phys., 34, 178.

Emslie, A. G. 1980, Ap. J., 235, 1055.

1981, Ap. J., 244, 653.

Gluckstern, R. L., and Hull, M. H. 1953, Phys. Rev., 90, 1030.

Gluckstern, R. L., Hull, M. H., and Breit, G. 1953, Phys. Rev., 90, 1026.

Haug, E. 1972, Solar Phys., 25, 425.

Henoux, J. C. 1975, Solar Phys., 42, 219.

Hoyng, P., and Melrose, D. B. 1977, Ap. J., 218, 866.

Hoyng, P. et al. 1981a, Ap. J. (Letters), 244, L153.

1981b, Ap. J. (Letters), 246, L155.

Hudson, H. S. 1972, Solar Phys., 24, 414.

Kane, S. R. 1974, in I.A.U. Symposium 57, Coronal Disturbances, ed. G. Newkirk (Dordrecht: Reidel).

Kane, S. R. 1980, Ap. Space Sci., 75, 163.

Kane, S. R., Anderson, K. A., Evans, W. D., Klebesadel, R. W., and Laros, J. G. 1979, Ap. J. (Letters), 233, L151.

Kane, S. R. et al. 1980, in Proc. 2d Skylab Workshop, Solar Flares (Team 4 Rept.), ed. P. A. Sturrock (Boulder, Colo.: University of Colorado Press).

Kane, S. R., Fenimore, E. E., Klebesadel, R. W., and Laros, J. G. 1982, Ap. J. (Letters), 254, L53.

Knight, J. W., and Sturrock, P. A. 1977, Ap. J., 218, 306.

Langer, S. H., and Petrosian, V. 1977, Ap. J., 215, 666.

Leach, J., and Petrosian, V. (paper 1) 1981, Ap. J., 251, 781.

Petrosian, V. 1973, Ap. J., 186, 291.

Petrosian, V. 1982, Ap. J., 255, L85.

Santangelo, N., Horstman, H., and Horstman-Moretti, E. 1973, Solar Phys., 29, 143.

Smith, D. F., and Brown, J. C. 1980, Ap. J., 242, 799.

Smith, D. F., and Lilliequist, C. G. 1979, Ap. J., 232, 582.

Tindo, I. P., Shuryghin, A. I., and Steffen, W. 1976, Solar Phys., 46, 219.

Van Beek, H. F. et al. 1980, Solar Phys., 65, 39.

1981, Ap. J. (Letters), 244, L157.

FIGURE CAPTIONS

Figure 1 The magnetic field structure which we use for the models. The loop is semicircular in the corona and vertical throughout the thin transition zone and the chromosphere. The loop is divided into several segments with a mean magnetic field direction $\underline{B}_i$. Also shown is an electron of momentum $\underline{p}$ injected into the loop at $\tau = 0$ and spiralling along the magnetic field. μ is the cosine of the pitch angle, the angle between the direction $\hat{B}$ of the magnetic field and $\hat{p}$ of the electron momentum.

Figure 2 The global observational frame with the z direction being vertically outward from the surface of the sun and the flare loop in the $\underline{y},\underline{z}$ plane. A photon $\underline{k}$ is shown emitted in the θ , Φ direction.

Figure 3 X-ray spectra in the x, y and z directions for model 3 (solid lines) and model 5 (dashed lines). The differences between the spectral indices of models 3 and 5 in each direction are small and are less than the uncertainties encountered in fitting a best-fit power law to the data. The spectral indices in the x, y and z directions are 4.4, 4.4 and 4.85, respectively.

Figure 4 X-ray directivity as a function of the polar angle θ . Zero degrees is the vertical direction away from the photosphere. Shown are the results for models 3 (solid lines), 5 (dashed lines) and 9 (dotted lines) at photon

energies of 22 keV (upper curves) and 210 keV (lower curves).

Figure 5 X-ray polarization as a function of the polar angle θ. Zero degrees is the vertical direction away from the photosphere. Shown are the results for models 3, 5 and 9 at photon energies 16, 50 and 102 keV.

Figure 6 X-ray spectrum at four positions throughout the loop and for the whole loop (dashed lines), for models 1, 3, 5 and 9 as marked in the top righthand corner of each box. The four solid lines in each box correspond to segments 1, 5, 7, and 9 at column depth of 3.4 (+17) cm^{-2} [τ = 6.8 (-6)], 2.6 (+18) cm^{-2} [τ = 5.1 (-5)], 1.3 (+20) cm^{-2} [τ = 2.5 (-3)] and 4.6 (+21) cm^{-2} [τ = 9.2 (-2)], respectively. The lines are separated to show the evolution of the spectrum with increasing depth, and their vertical positions do not correspond to the relative x-ray intensity at each depth.

Figure 7 The fraction of the total number of counts emitted per unit column depth, $I(k, \tau)$, against τ, at 16 and 50 keV for models 1 (δ = 3), 2 (δ = 4) and 3 (δ = 5). At large values of τ the slopes $d[\ln I(k,\tau)]/d\ln\tau = -\delta/2$ and are independent of energy.

Figure 8 As Figure 7, but for models 3 ($\alpha_o^2 = \infty$), 4 ($\alpha_o^2 = 0.4$) and 5 ($\alpha_o^2 = 0.04$). At large values of τ the slopes are independent of α_o^2.

Figure 9 As Figure 7, but for models 4 ($d\ln B/d\tau = 0$), 6 ($d\ln B/d\tau = 2.5 \times 10^4$) and 7 ($d\ln B/d\tau = 5 \times 10^4$). The transition zone is marked in at $\tau = 6.3$ (-5) [$N_{TZ} = 10^{18.5}$ cm^{-2}].

Figure 10 The directivity $I(k,\theta,\phi)/\bar{I}(k)$ as a function of θ for $\phi = 90^o$ (the x direction) at four heights and at two energies, 16 keV and 102 keV, for model 5. θ is the polar angle in the local observation frame, and zero degrees is always into the upward-looking hemisphere, that is, away from the photosphere. The curves are labeled according to the segment of the loop to which they rerer. Segment 1 is at the top of the coronal loop and has an average column depth of 3.4 (+17) cm^{-2} [τ = 6.8 (-5)], segment 5 is the transition zone at a column depth of 3.2 (+18) cm^{-2} [τ = 6.4 (-4)], segments 7 and 9 are in the chromosphere at column depths of 1.3 (+20) cm^{-2} [τ = 2.5 (-3)] and 4.6 (+21) cm^{-2} [τ = 9.2 (-2)], respectively. Also shown is the directivity for the whole loop at these two energies.

Figure 11 The same as Figure 10, but for the degree of linear polariation.

Figure 12 As Figure 11, but for model 3. Note the different scale from Figure 11.

Figure 13 As Figure 12, but for model 8.

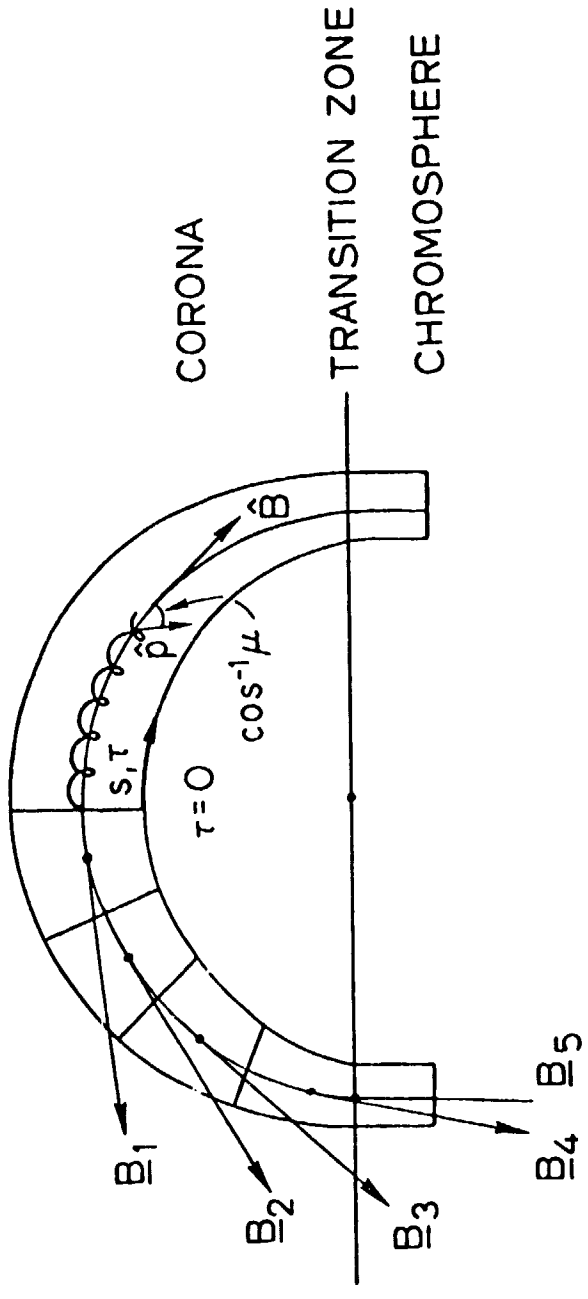

Figure 1

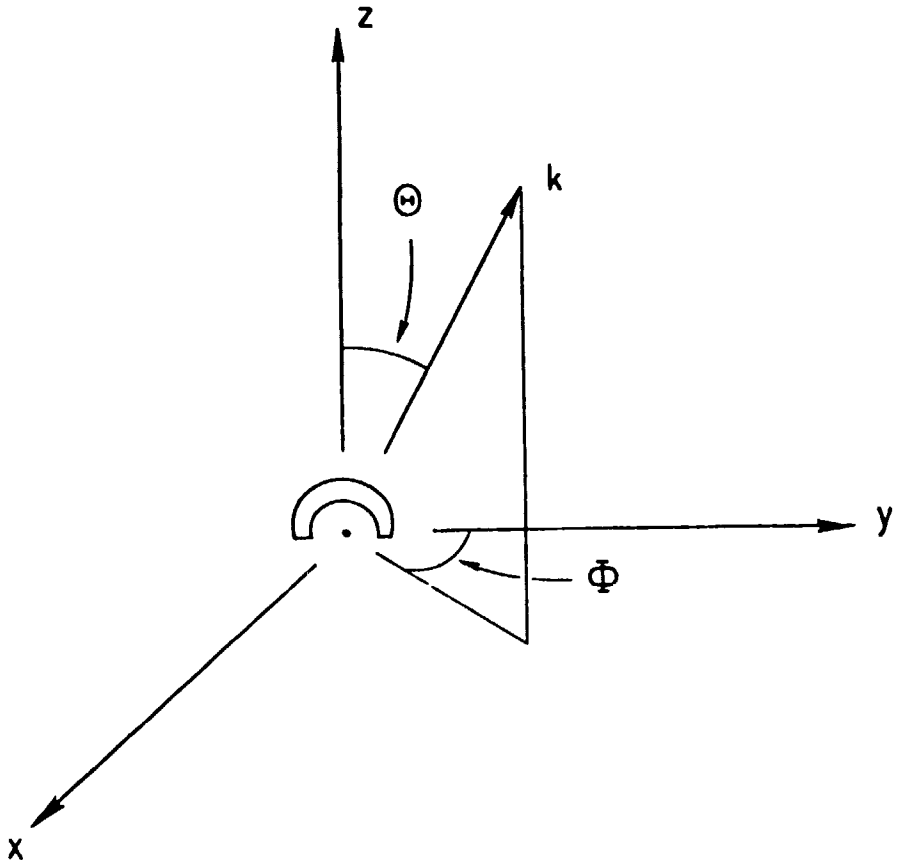

Figure 2

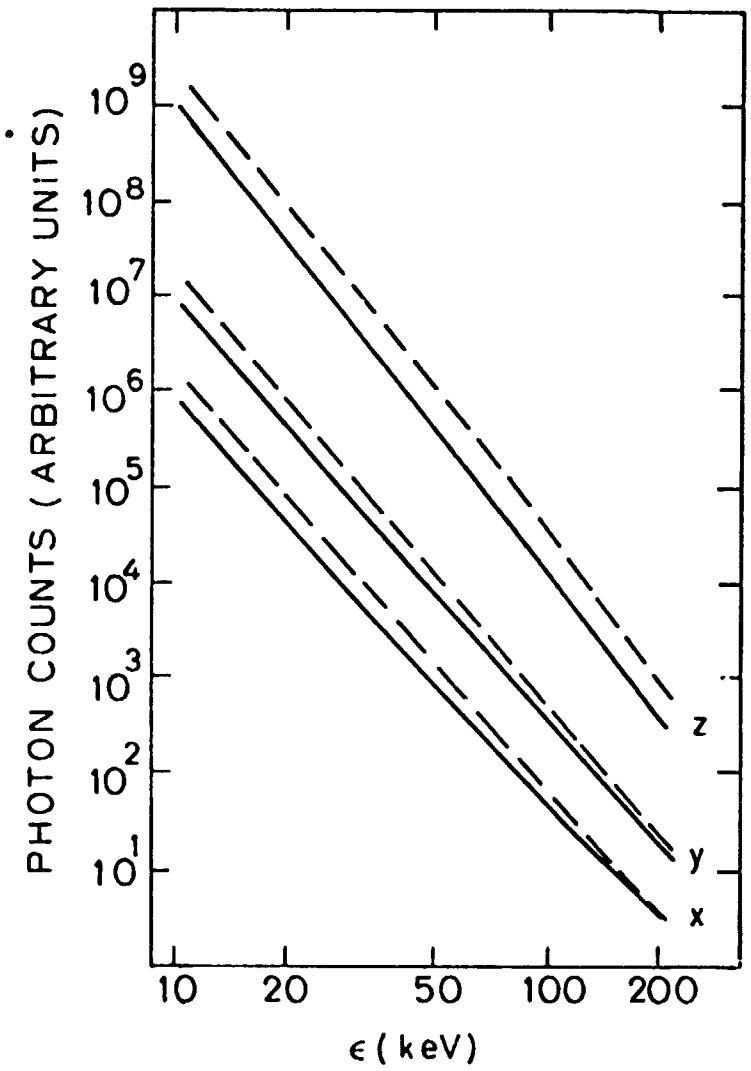

Figure 3

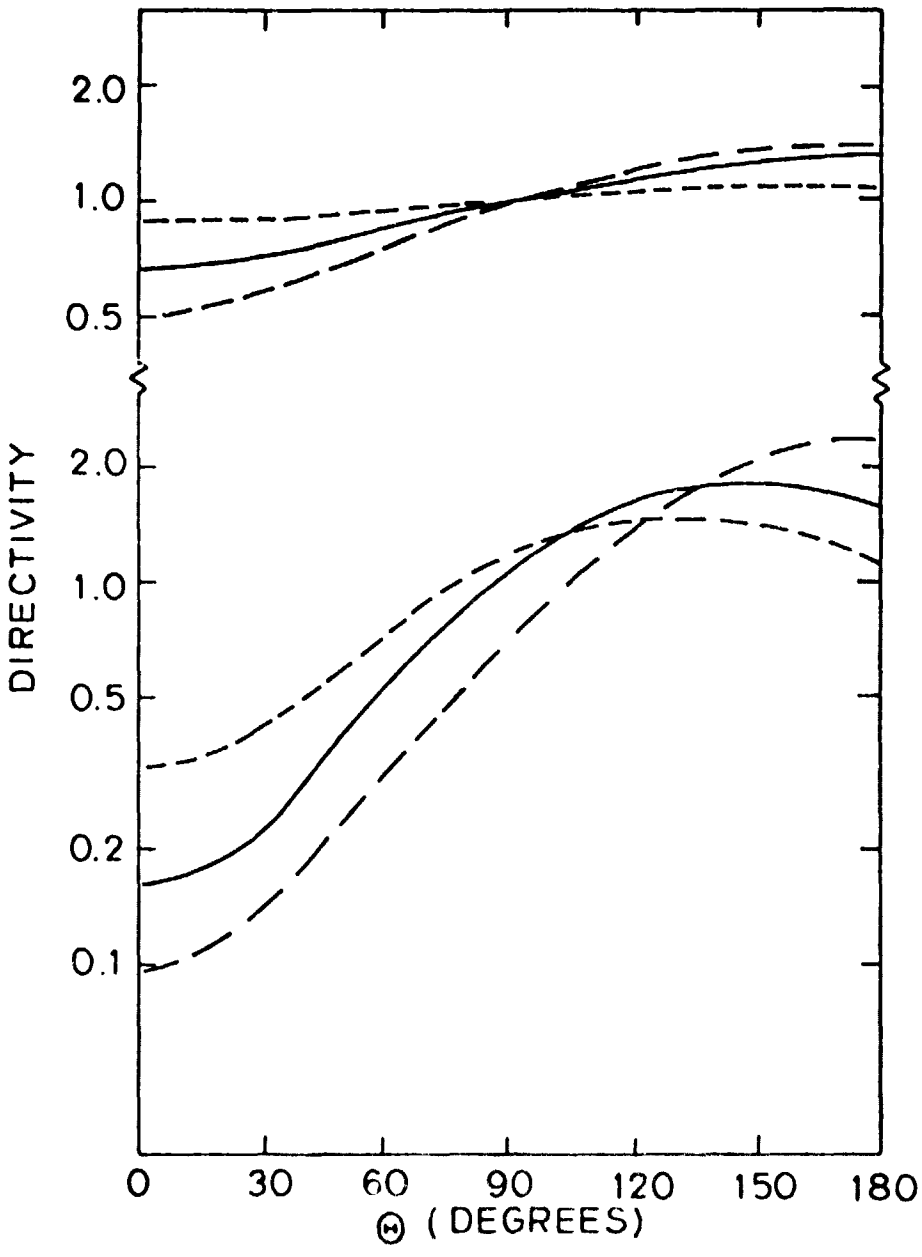

Figure 4

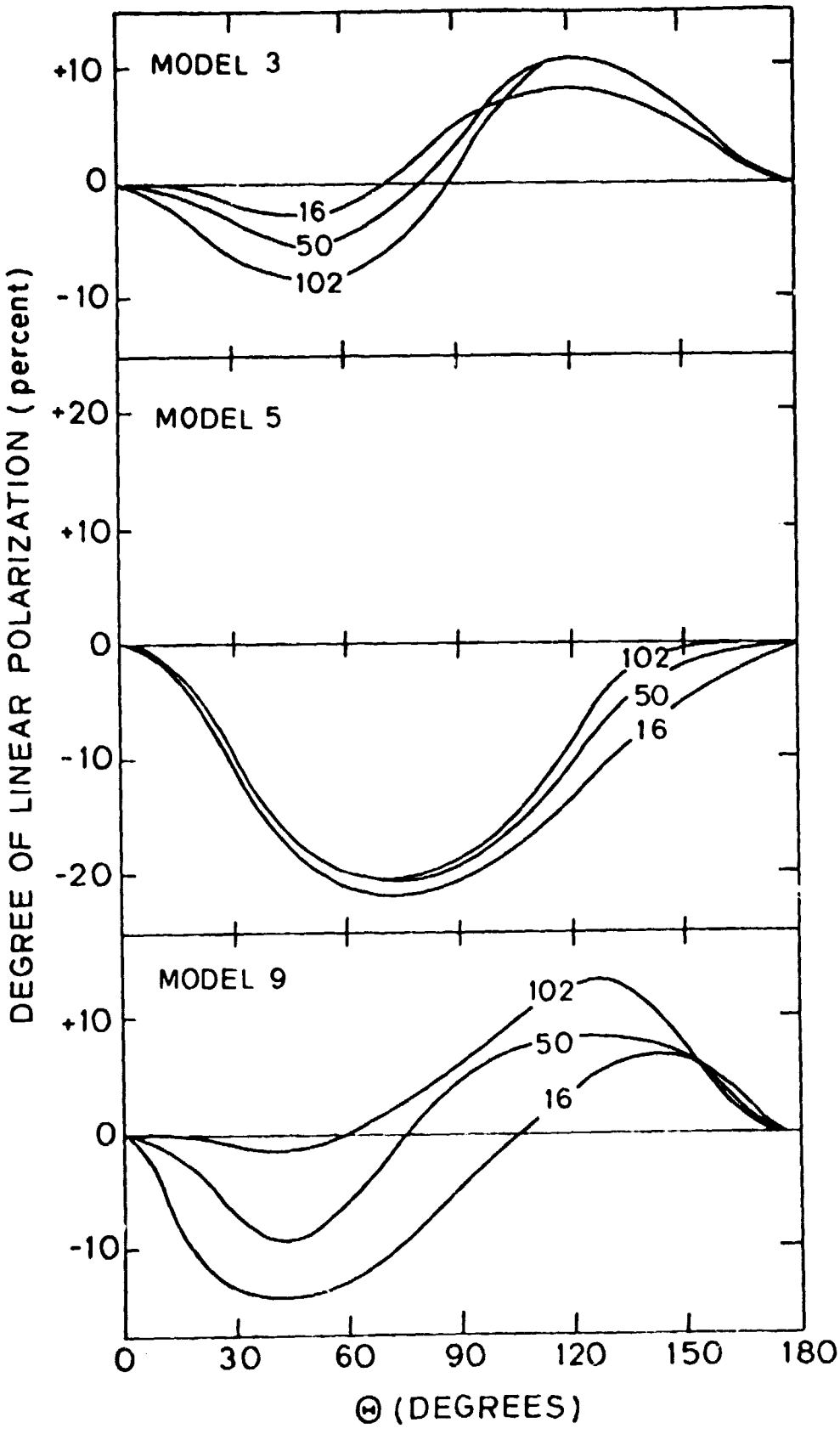

Figure 5

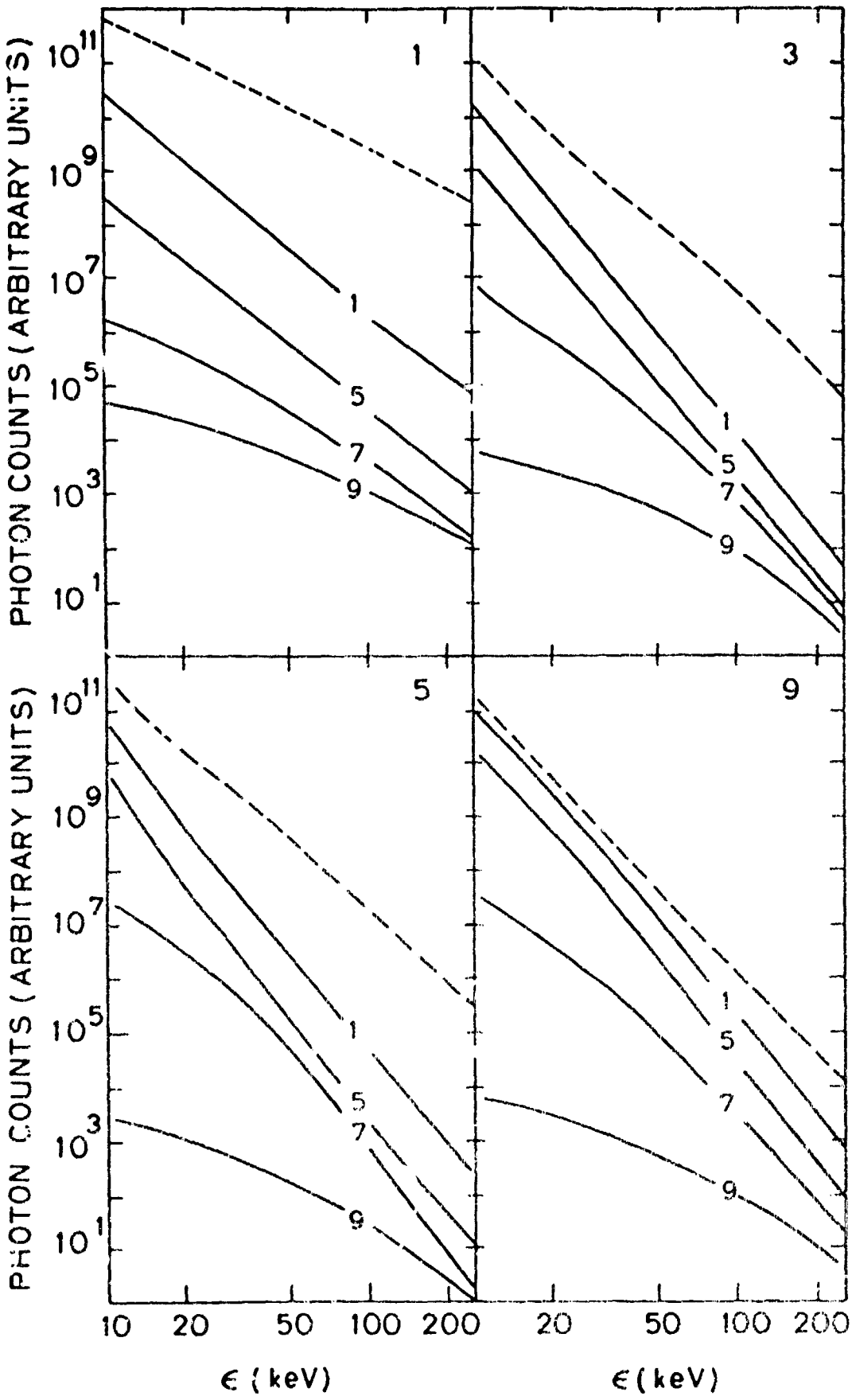

Figure 6

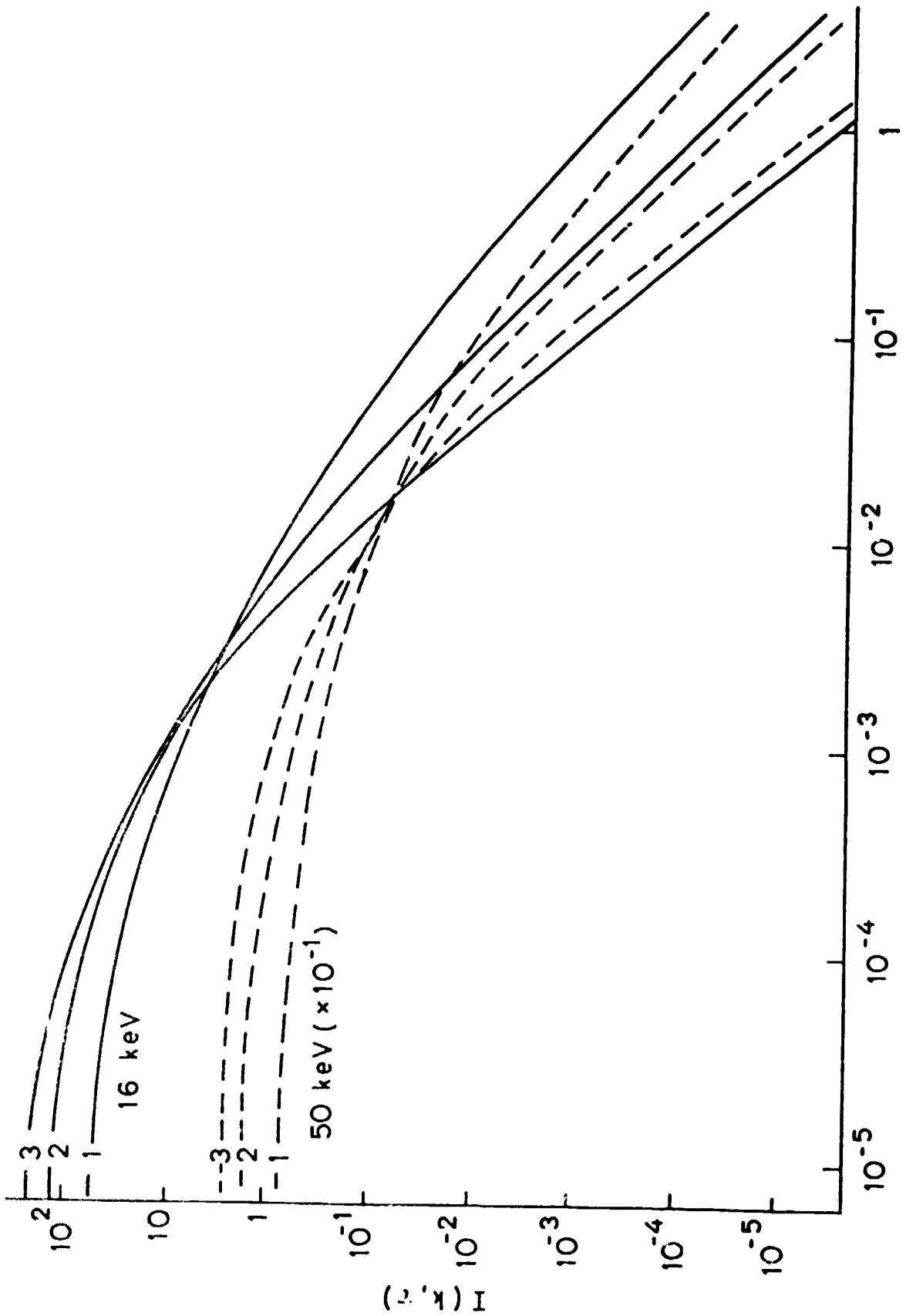

Figure 7

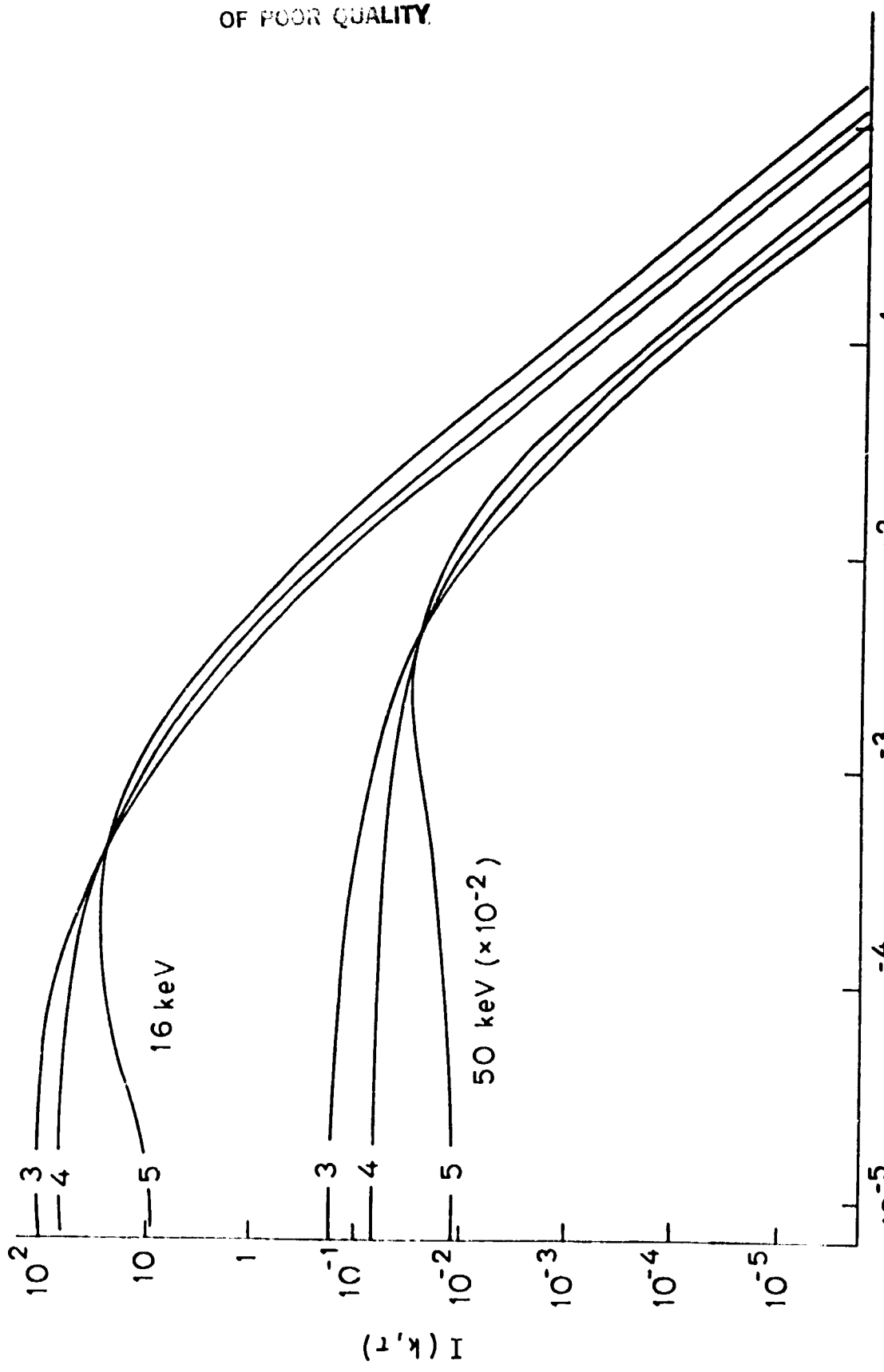

Figure 8

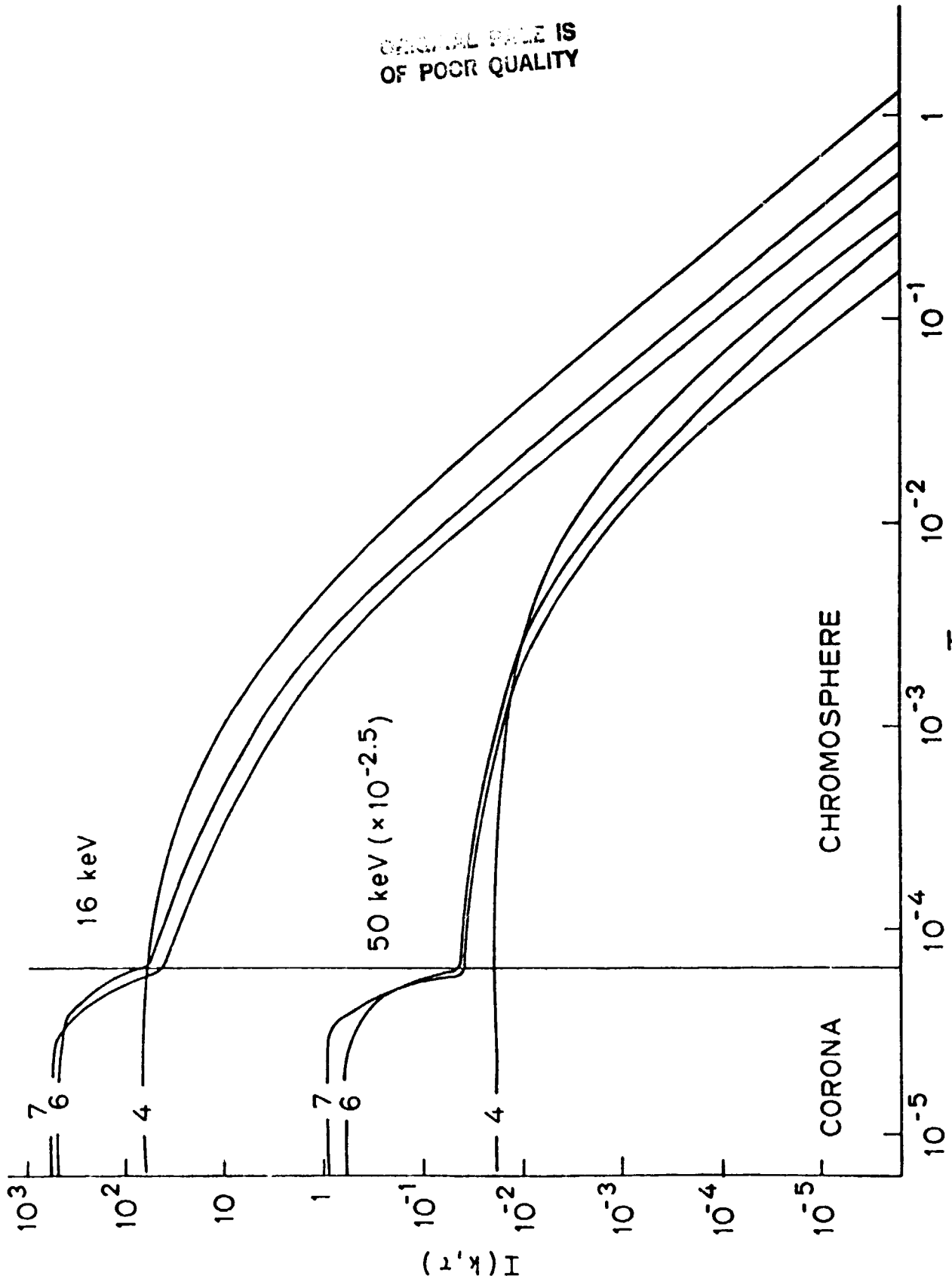

Figure 9

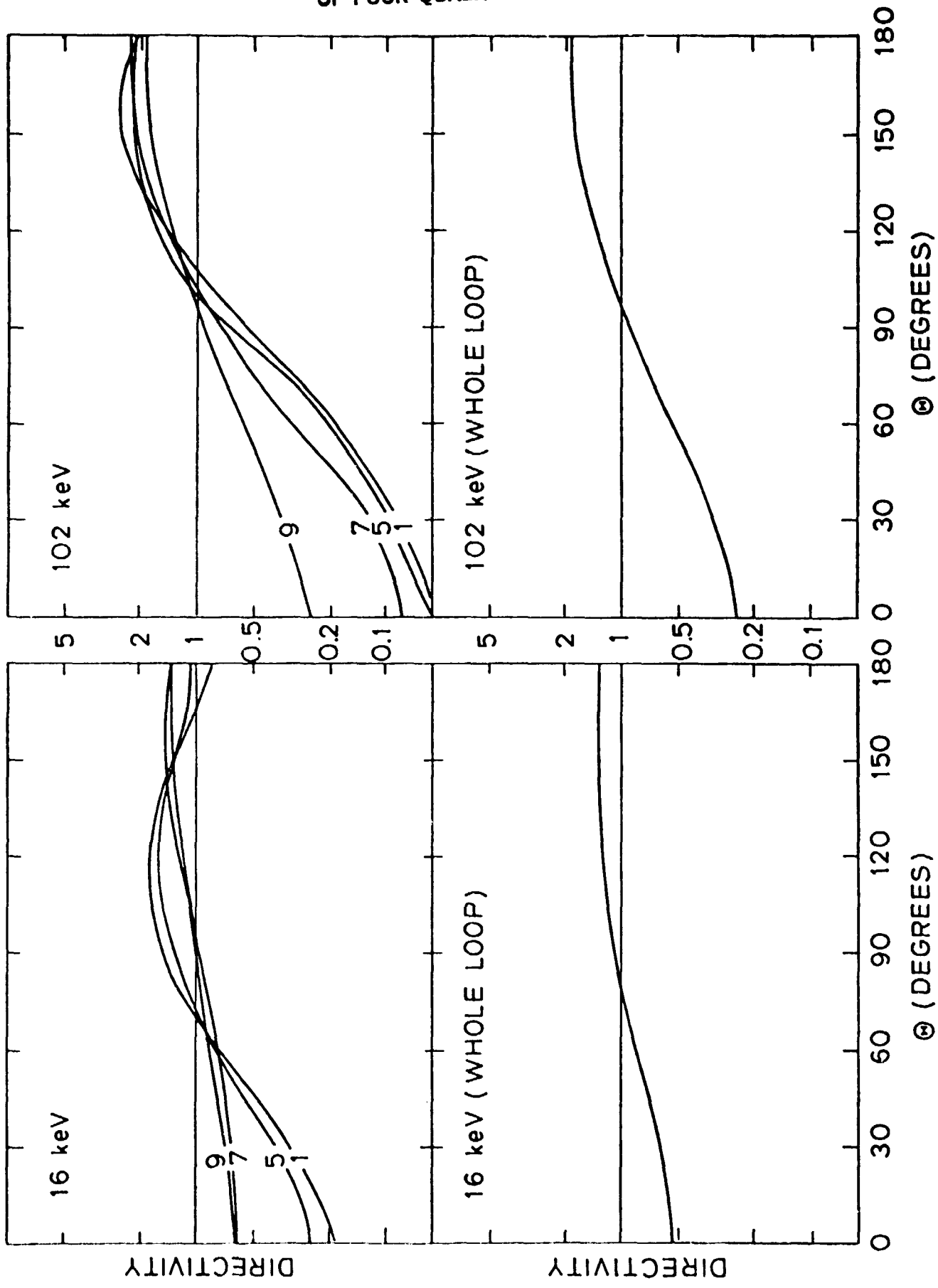

Figure 10

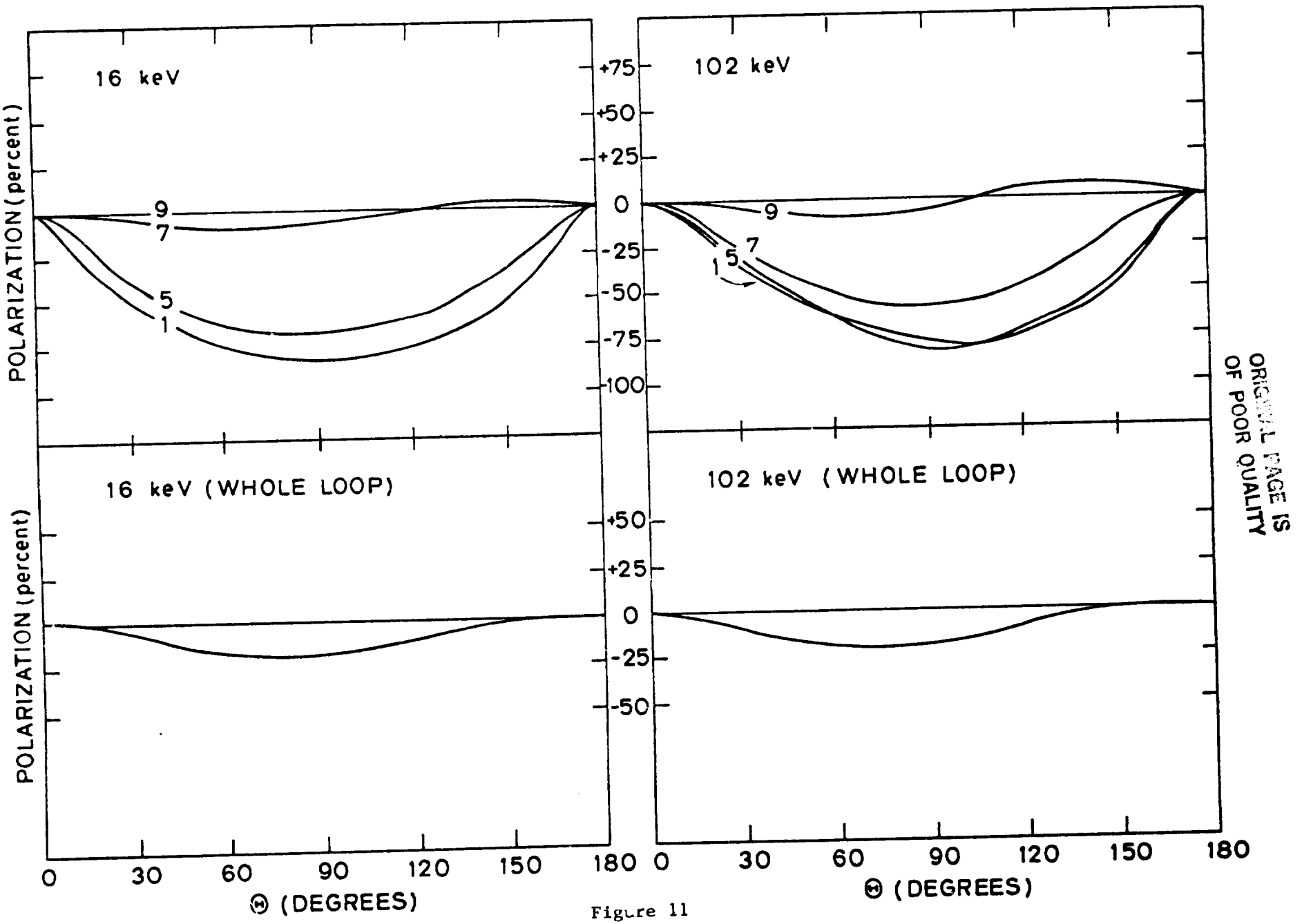

Figure 11

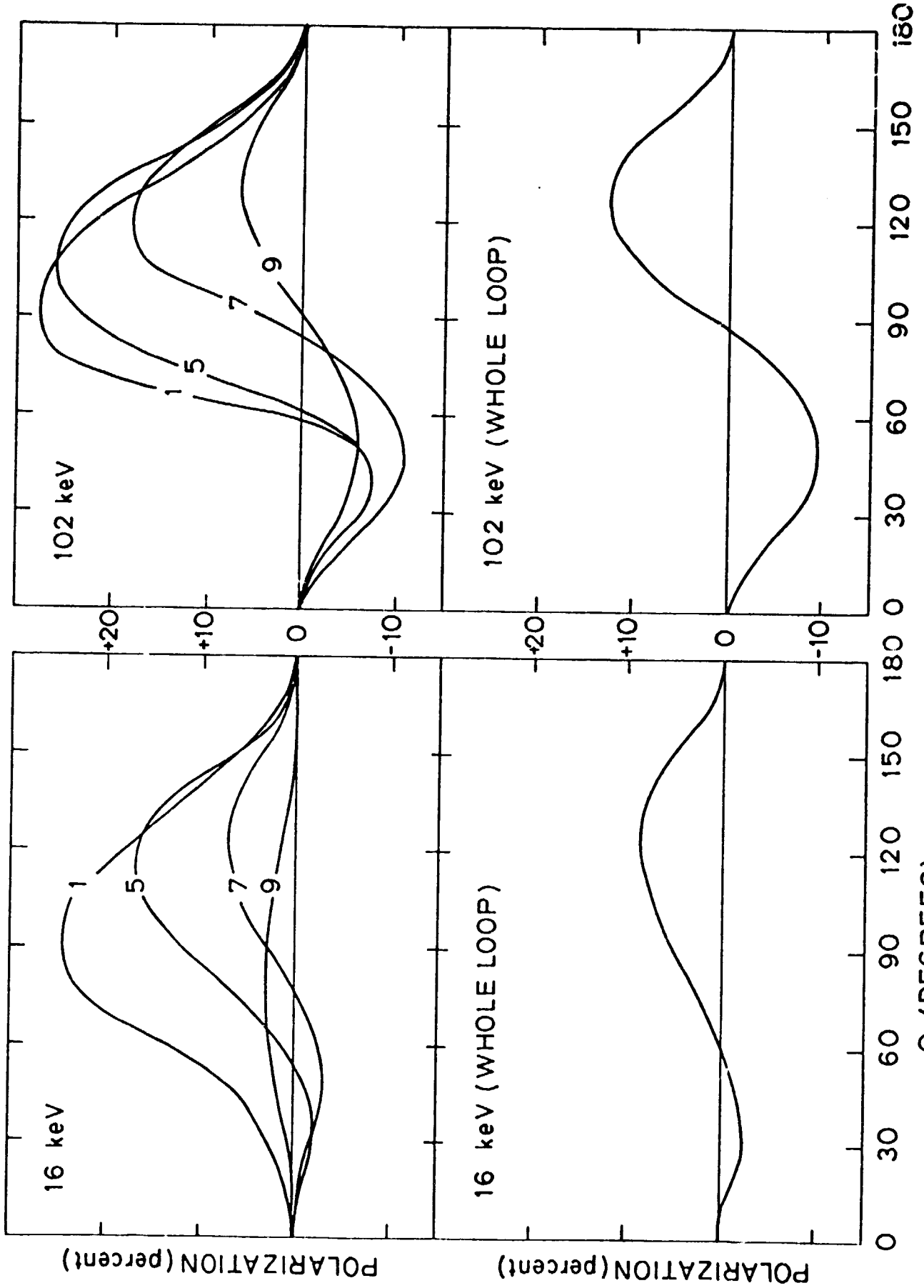

Figure 2

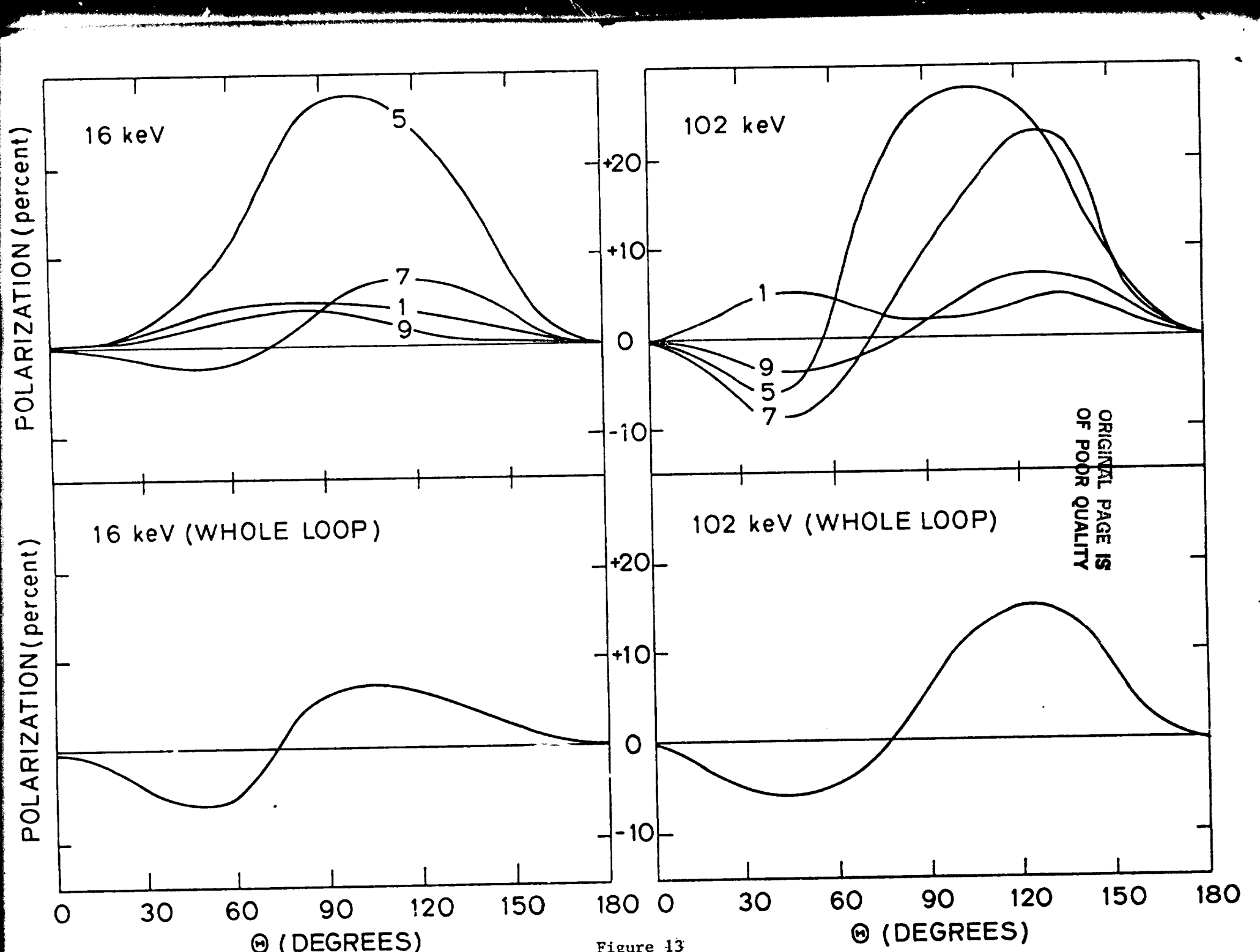

Figure 13